Theory of melt fracture instabilities in the capillary flow of polymer melts

Joel D. Shore,[1,*] David Ronis,[1,2] Luc Piché,[1,3] and Martin Grant[1]

[1]*Department of Physics and Centre for the Physics of Materials, McGill University, 3600 University Street, Montréal, Québec, Canada H3A 2T8*

[2]*Department of Chemistry, McGill University, 801 Sherbrooke Street West, Montréal, Québec, Canada H3A 2K6*

[3]*Industrial Materials Institute, National Research Council of Canada, 75 De Mortagne Boulevard, Boucherville, Québec, Canada J4B 6Y4*

(Received 1 July 1996)

We present a model for the flow of a polymer melt through a capillary with nonlinear slip boundary conditions at the wall of the capillary. The model consists of the linearized Navier-Stokes equations coupled to a Maxwell constitutive relation for the viscoelasticity and a phase-field model for a first-order transition between stick and slip flow at the boundary. Specializing to the case of a two-dimensional capillary, we perform a linear stability analysis about the steady-state solutions and predict in which parameter regimes the steady-state becomes unstable. A numerical study of the model shows regions of steady flow, as well as regimes with periodic oscillations, spatially uniform but temporally chaotic oscillations, and more complicated spatiotemporal behavior. We show that the oscillations can account for the sharkskin texturing and defect structures seen in the extrusion of polymer melts. [S1063-651X(97)10401-9]

PACS number(s): 61.25.Hq, 83.20.Lr, 64.60.My, 47.50.+d

I. INTRODUCTION

Understanding the instabilities which occur when a polymer melt is extruded through a capillary (or ''die'') is a longstanding problem in the plastics and chemical engineering communities. The issue was of large technological importance for the plastics industry in the 1950s and 1960s since these instabilities lead to unwanted distortions in the final plastic product, which have been collectively termed ''melt fracture.'' Over time, engineers have found ways to avoid or minimize the problem in practice, but little understanding of the origin of these distortions has been reached and much discussion of the problem has continued in the rheology and non-Newtonian fluid mechanics literature. For recent reviews, see [1,2].

The problem can best be described by reference to the sketch of the ''flow curve'' presented in Fig. 1. (For actual experimental curves, see, e.g., Refs. [1–4].) The horizontal axis specifies the apparent shear rate of the polymer melt at the wall of the capillary [5], while the vertical axis specifies the shear stress at the wall. (Shear rate and shear stress, although the more fundamental quantities, are not the most directly accessible; in terms of physically measurable or controlable parameters, the horizontal and vertical axes correspond to the flow rate and the applied pressure, respectively.) The inset in Fig. 1 is a cartoon of a typical experimental setup: a piston or screw feeds the polymer melt into a reservoir and eventually through the die and out the other end, where it cools and solidifies.

As the flow rate in the die is increased, one typically finds several different regimes [2,3,6]: At the lowest flow rates, the extrudate is smooth and regular. Next, one encounters a regime of surface distortion termed ''sharkskin,'' in which the extrudate develops a sawtooth texturing on its surface. Often a change in the slope of the flow curve is apparent near the onset of the sharkskin, as shown in Fig. 1. At still larger flow rates, one sees ''stick-slip'' or ''spurt'' flow, which is characterized by fairly long time oscillations in the flow rate (e.g., on the order of seconds), with a noticeable effect on the extrudate. Sharkskin is frequently seen on the extrudate during all or part of the stick portion of the cycle. Finally, at the highest flow rates, one sees ''gross'' or ''wavy'' melt fracture which is characterized by a highly irregular extrudate. Not all these regimes are necessarily seen for all materials and, in particular, the ''stick-slip'' or ''spurt'' flow is seen only in those experimental setups where it is the piston speed, rather than the pressure, which is held fixed. Under pressure regulation, one instead sees hysteresis, where on increasing and decreasing pressure the flow rate jumps when limits of metastability are reached, as shown by the dashed lines and arrows in Fig. 1.

There has long been controversy about whether these effects are due to instabilities inside the die, or are instead due to instabilities at the die entrance or exit, or some combinations of these. However, recent ultrasonic measurements [7] show that anomalous time-dependent behavior in the polymer flow occurs within the die, far from both the entrance and exit (and even at flow velocities somewhat below those where sharkskin first becomes apparent), thus suggesting that instabilities inside the die itself are probably important.

Since the Reynolds number [8] is still very small when these instabilities occur, it is clear that they cannot be due to turbulence in the die; hence, the instabilities are most likely to be due to some of the special properties of polymer melts, which of course differ from classical fluids in a number of important ways [9]. First, the time scales for relaxation are long and widely distributed. Therefore, the fluids can behave elastically on laboratory time scales and must be modeled with *viscoelastic* constitutive relations between the stress and strain. Second, the viscosity in the fluids is often found to be

*Current address: Bldg. 83, 2nd floor, RL, Eastman Kodak Company, Rochester, NY 14650-2216.

 © 1997 The American Physical Society

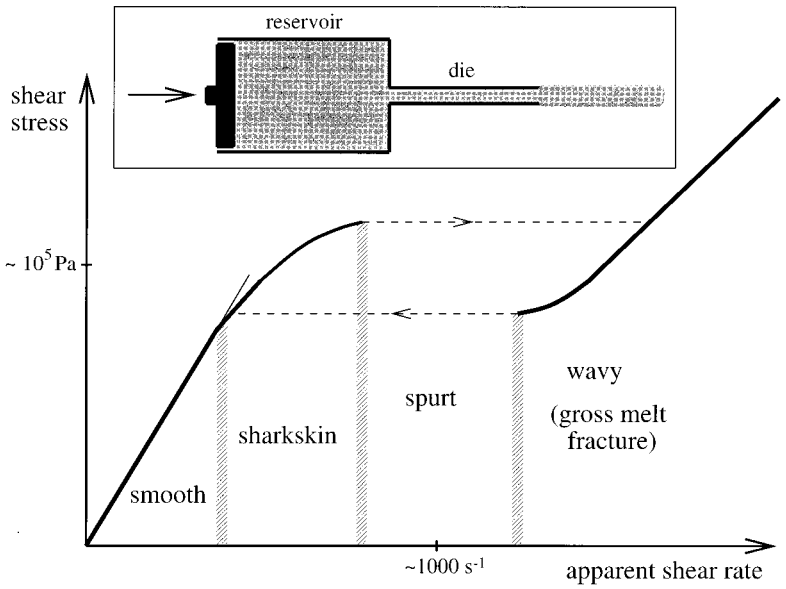

FIG. 1. Sketch of a typical flow curve seen in experiments on extrusion of polymer melts, adapted from [2–4]. Shown is the shear stress at the wall, $\sigma_{xy}^{\text{wall}}$, as a function of the shear rate, e_{xy}^{wall}, at the wall. Also shown are the approximate flow regimes where different imperfections are seen on the extrudate. For photographs of the extrudate produced in these regimes, see [1]. In the spurt regime, the flow oscillates in time; alternatively, if the experiment is performed at constant pressure, this regime is not accessible and hysteresis is seen instead, as shown by the horizontal dashed lines. The inset shows a typical experimental setup where the melt is pushed by a piston from a large reservoir through the capillary and out the other end where it solidifies.

a decreasing function of the shear rate, a phenomenon termed ''shear-thinning.'' The proposed explanation of this is that under larger shears the polymers tend to line up parallel to the flow and can then more easily slide past one another.

Third, there is increasing evidence that polymeric fluids might not obey the ''stick'' boundary condition at the walls of the container that is standardly assumed in hydrodynamics. That slip behavior could occur in polymer melts was suggested in some of the earliest literature on melt fracture [10]; such ideas were introduced into the physics community several years ago by de Gennes [11]. More recently, de Gennes and co-workers have expanded on this idea, suggesting that a sharp transition should occur between stick and slip behavior as the shear rate at the walls is increased [12]. Experimental evidence for the importance of slip has been accumulating in the study of polymer melts [1,2,13,14], and although most of the evidence has been rather indirect, a recent elegant experiment by Migler *et al.* [15] using a polymeric fluid in the planar Couette geometry [8] actually measured the velocity of the fluid within 100 nm of the wall, confirming much of de Gennes' picture. In particular, the authors found that as the shear rate was increased there was a sharp transition at which the slip velocity jumped by about four orders of magnitude.

In order to understand the phenomenon of melt fracture, we present a hydrodynamic model that describes the flow of a viscoelastic fluid in which the polymer near the surface undergoes a first-order transition in conformation as a function of the shear stress at the wall. This conformational change leads to a change in the frictional force between the wall and the polymer in the bulk, producing stick-slip behavior, and leading in a natural way to an effectively multivalued flow curve [see Fig. 2(a)], as has been much discussed in the recent literature [1,2,16,17]. When the die is coupled to a large reservoir in which the polymer can be compressed, we find that the multivalued flow curve gives rise to oscillatory spurt flow, as has been discussed previously [2]. More significantly, and even in the absence of the effect of the reservoir, we find that the *elastic* nature of the fluid can give rise to periodic oscillations, chaotic behavior, and large-scale spatial structures in the die, which we conjecture is responsible for sharkskin. A shorter communication of our work has been presented in Ref. [18]. Here, we give a fuller description of the model, discuss the determination of the steady-state solution and the exact linear stability analysis about this solution, and give much more detail of the numerical results and relation to experiment.

The plan of the paper is as follows: In Sec. II, we present the basic elements of our model and discuss the Fourier transform of the fluid flow equations to reexpress the model in a mixed spectral and real space representation. In Sec. III, we examine the steady-state solutions and their linear stabil-

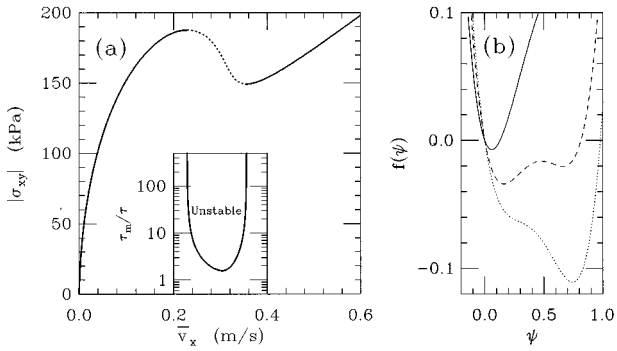

FIG. 2. (a) Flow curve for our model produced using the parameter values given in Table I. Shown is the shear stress at the wall, $\sigma_{xy}^{\text{wall}}$, as a function of the average flow velocity, $\overline{v_x}$ in steady state. Each point on this curve is associated with a uniform steady-state solution of the model. The dotted part of the curve has $\overline{\chi}^{-1}<0$ and is thus *potentially* unstable, while the solid part has $\overline{\chi}^{-1}>0$ and is stable. The inset shows the range of $\overline{v_x}$, where the steady-state solution is actually found to be linearly unstable as a function of τ_m/τ, as obtained from an approximate result of the linear stability analysis, Eq. (3.24). (b) Local free energy density $f(\psi)$ for three different values of $\sigma_{xy}^{\text{wall}}$. The solid, dashed, and dotted curves are for shear stresses of $\sigma_{xy}^{\text{wall}} = 80$, 160, and 200 kPa, respectively. The dashed part of the flow curve in (a) corresponds to a maximum in $f(\psi)$ while the solid part of the curve corresponds to minima in $f(\psi)$.

ity. In Sec. IV, we present numerical results, first briefly discussing the numerical method, next considering oscillatory solutions which are spatially uniform in the flow direction, and then considering spatially nonuniform solutions. We conclude Sec. IV with a discussion of two additional features which must be added to the model in order to fully reproduce features seen in most experiments: compressibility of the melt in the reservoir and nonuniformity in the boundary conditions along the walls. Finally, in Sec. V, we conclude with a summary and a brief discussion of avenues for future research.

II. THE MODEL

A. General presentation

We consider Poiseuille (pipe) flow [8] in a circular or rectilinear geometry. Generalization to more complicated geometries or to other types of flows, such as planar or cylindrical Couette flow [8] is straightforward. We assume periodic boundary conditions in the flow direction and impermeable walls on the sides of the capillary.

The bulk fluid flow is specified by the following equations:

$$\rho \frac{\partial \mathbf{v}(\mathbf{r},t)}{\partial t} = -g(t)\hat{\mathbf{x}} - \nabla \delta p(\mathbf{r},t) + \nabla \cdot \overleftrightarrow{\sigma}(\mathbf{r},t), \tag{2.1}$$

$$\nabla \cdot \mathbf{v}(\mathbf{r},t) = 0, \tag{2.2}$$

and

$$\tau_m \frac{\partial \overleftrightarrow{\sigma}(\mathbf{r},t)}{\partial t} = -[\overleftrightarrow{\sigma}(\mathbf{r},t) - \eta_0 \overleftrightarrow{e}(\mathbf{r},t)]. \tag{2.3}$$

Equation (2.1) is the Navier-Stokes equation [8], which is simply Newton's law for the velocity $\mathbf{v}(\mathbf{r},t)$ of a fluid element at position $\mathbf{r}$ and time t with density ρ. $\overleftrightarrow{\sigma}(\mathbf{r},t)$ is the (viscous) stress tensor. The pressure term has been divided into two parts: $p(\mathbf{r},t) = g(t)x + \delta p(\mathbf{r},t)$, where $g(t)$ is a uniform pressure gradient in the flow direction, and $\delta p(\mathbf{r},t)$ is the excess part, which (like all the other variables) is periodic in the x direction. Equation (2.2) is the continuity equation which follows from the assumption that the fluid is incompressible. In solving these equations, the incompressibility condition and the boundary condition that the perpendicular component of the velocity must go to zero at the walls are used to determine $\delta p(\mathbf{r},t)$. Equation (2.3) is the Maxwell constitutive relation for a linear viscoelastic fluid [9], with η_0 the viscosity and $\overleftrightarrow{e}$ the rate of strain tensor with components $e_{ij} \equiv \partial v_i/\partial x_j + \partial v_j/\partial x_i$. By varying the Maxwell relaxation time, τ_m, we can tune between a viscous fluid ($\tau_m \to 0$) and an elastic solid ($\tau_m, \eta_0 \to \infty$).

These three equations together constitute a standard hydrodynamic model for an incompressible viscoelastic fluid [9]. Note, however, that we have linearized the equations by replacing the total or convective derivatives that would normally appear on the left-hand side of Eqs. (2.1) and (2.3) with a simple partial derivative. This is an excellent approximation for Eq. (2.1) because the instabilities we will study are found to occur at very low Reynolds number [8], where these terms are very small. For Eq. (2.3), the corresponding dimensionless ratio to consider is the Weisenberg number, given by the product of the shear rate and τ_m. This is estimated to be of order 0.1 to 1 in the range where sharkskin and spurt flow are seen. Because the convective terms identically vanish for flows that are uniform in the flow direction, we expect that, in analogy with the Reynolds number, the Weisenberg number generally has to be considerably larger than one before the convective terms become important. These terms do play a role in certain cases, such as in producing higher stresses near the ends of the die (as will be discussed in Sec. IV C) and for the behavior at higher flow rates, i.e., in the gross melt fracture regime not studied in this paper. In this regard, we note that a recent paper by Black and Graham [19] argues that there exists a *large*-wavenumber instability when terms in their model, analogous to those proportional to the Weisenberg number discussed above, are large (that is, for high shear rates). However, here we believe that the most important nonlinearities in the problem come in through the boundary conditions at the walls of the die. (We could also add additional nonlinearities by including shear thinning [9] in our model; however, preliminary investigations showed that considering such a complication was not necessary to produce the physics of interest here.)

The boundary condition for the fluid velocity at the walls of the die is coupled to the kinetics of a first-order phase transition [20] describing the conformation of the polymer at the wall by the following equations:

$$\mathbf{v}_\parallel(\mathbf{r}=\mathbf{r}_\parallel,t) = \ell \psi(\mathbf{r}_\parallel,t)(\hat{\mathbf{n}} \cdot \nabla \mathbf{v}_\parallel)\big|_{\mathbf{r}=\mathbf{r}_\parallel}, \tag{2.4}$$

$$F[\psi] = \int_{\text{walls}} d\mathbf{r}_\parallel \left[f(\psi) + \frac{\xi_0^2}{2} (\nabla_{\mathbf{r}_\parallel} \psi)^2 \right], \tag{2.5}$$

and

$$\tau \frac{\partial \psi(\mathbf{r}_\parallel,t)}{\partial t} = -\frac{\delta F}{\delta \psi(\mathbf{r}_\parallel,t)}. \tag{2.6}$$

Equation (2.4) specifies the slip boundary condition, with the slip velocity assumed to depend on the shear rate at the wall [21]. Here, $r_\parallel$ denotes a coordinate which ranges only over the walls, $\hat{\mathbf{n}}(\mathbf{r}_\parallel)$ is defined as the inward unit normal at the wall, and $\mathbf{v}_\parallel(\mathbf{r}_\parallel,t) \equiv v_\parallel(\mathbf{r}_\parallel,t)\hat{\mathbf{v}}_\parallel(\mathbf{r}_\parallel,t)$ is the component of the fluid velocity parallel to the wall. ℓ is a constant with the dimensions of length and ψ is a dimensionless quantity defined locally at each point $\mathbf{x}$ along the walls at time t. Equation (2.4) defines a slipping length, $\ell\psi$, which has the geometric interpretation as the distance between the die wall and the point *outside* the die at which the tangential velocity, linearly extrapolated based on its value and the value of its gradient at the wall, would go to zero. In particular, $\ell\psi \to 0$ corresponds to ''stick'' (tangential velocity zero at the wall) while $\ell\psi \to \infty$ corresponds to perfect slip. Equation (2.4) is an equation commonly used to describe slip boundary conditions [1,12–15]; our one generalization here is to assume that the slipping length is a local quantity which can be specified at each point along the wall.

Experiments show that the slipping length jumps sharply at a critical value of the shear [13,15], while hysteresis is observed on the multivalued flow curves seen in extrusion

[1,2]. Together, these two features suggest the change in slipping length is the nonequilibrium analogue of a first-order phase transition, presumably the result of a transition in the local conformational state of the polymer at the wall. Equation (2.5) presents the free energy functional of a Ginzburg-Landau phase-field model [22] for $\psi(\mathbf{x},t)$. We consider a standard ψ^4 free energy model with local free energy density

$$f(\psi)=\frac{c}{4}\psi^4-\frac{b}{3}\psi^3+\frac{a}{2}\psi^2-(H\hat{\mathbf{v}}_\parallel\cdot\overleftrightarrow{\sigma}\cdot\hat{\mathbf{n}})\psi. \qquad (2.7)$$

Note the inclusion of a linear term coupling $\psi(\mathbf{x},t)$ to the value of the shear stress, $\hat{\mathbf{v}}_\parallel\cdot\overleftrightarrow{\sigma}\cdot\hat{\mathbf{n}}$, at the wall. The second term in Eq. (2.5) is a square-gradient term which resists changes in $\psi(\mathbf{x},t)$ in the direction along the wall. The constants a, b, c, H, and ξ_0 are all taken to be positive, with the latter being a bare correlation length. With this choice of signs, and with the parameter values appropriately chosen [23], the equilibrium value of ψ is zero when $\sigma_{xy}=0$, with a first-order transition to a large value of ψ as the stress increases. The microscopic picture of de Gennes and coworkers [12] suggests associating larger ψ with the stretching and uncoiling of some polymers attached to the wall under the action of the shear stress, although it has been suggested that other mechanisms such as desorption of the polymer at the wall may be relevant [14], and in fact that the specific mechanism for the stick-slip transition might even vary from one system to another [13,14]. Our model is not dependent on a specific microscopic mechanism. Rather, in the spirit of keeping our model simple and general, we assume only that the change in conformation can be specified by its effect on the slipping length $\ell\psi(\mathbf{r}_\parallel,t)$ [24]. Note that, although our mesoscopic description is motivated by a microscopic picture, the collective gradient term proportional to ξ_0 is a feature particular to our treatment. Since such a term is the most simple allowed by symmetry, and naturally occurs in mesoscopic descriptions similar to ours, we expect that coarse graining or renormalizing the microscopic description will give rise to it. At any rate, we will find that the most complex spatiotemporal behavior occurs when ξ_0 is much smaller than the other length scales in the system.

Finally, Eq. (2.6) is an equation for dissipative relaxation of the polymer conformation toward states that are local minima in the free energy. The local rate of change of ψ is proportional to the functional derivative of the free energy with respect to ψ. The constant of proportionality is given by $1/\tau$ where τ is the characteristic time scale for relaxation of the polymer conformation [25]. In general, one would also include noise terms in these equations, with their amplitudes determined by fluctuation-dissipation relations [20,22]. However, for our purposes, these terms should be of minor importance and are neglected. It is through Eqs. (2.4)–(2.6) that nonlinearities enter our description; the equations for the bulk fluid, though viscoelastic, are linear. It is possible that a more complicated description of the dynamics of the polymer near the wall would be required to describe some processes of interest, but in the absence of any substantive justification, we have chosen as simple a model as the physics of the problem requires.

Having defined the model, it is now useful to summarize some of its basic features. The most important is the introduction of a first-order stress-induced phase transition for the conformation of the polymer at the wall. The conformational change couples back to the fluid flow by changing the slipping length at the wall. Since there is a range of values of $|\sigma_{xy}|$ where the local free energy density $f(\psi)$ has a double-welled structure, this gives rise to hysteresis associated with the spinodal part of the van der Waals loop in $\partial f/\partial\psi$, where the local susceptibility $\chi\equiv(\partial^2 f/\partial\psi^2)^{-1}$ is negative, while retaining consistency with a sharp first-order phase transition in the infinite-time limit. This hysteresis in the conformation of the polymer at the wall leads directly to hysteresis in the fluid flow because of the coupling of the polymer conformation to the slip length $\ell\psi$. Such hysteresis has indeed been seen experimentally, and much recent theoretical work has incorporated it in an *ad hoc* fashion [1,2,16,17], i.e., by positing a nonmonotonic relation between slip velocity and wall stress, and then assuming a history dependence in determining which slip velocity to use in the case where the curve is multivalued. Here, such hysteresis arises naturally from a well-accepted description of the dynamics of a first-order phase transition.

It is not obvious that the instability associated with the polymer conformation at the wall will necessarily lead to an instability of the entire fluid, and in fact, it might seem rather surprising that an instability at the wall could be so effective in driving an instability in a viscous fluid. We will see, in fact, in Sec. III B that the *elasticity* of the polymer melt plays a crucial role in determining whether or not the system is unstable: Only if the fluid is sufficiently elastic that it acts as a solid on the time scales over which the polymer conformation changes at the walls (i.e., if $\tau\lesssim\tau_m$) will the system be able to sustain oscillations [26]. However, before discussing the origin of the oscillations in the polymer melt in further detail, it is useful to rewrite the equations in a form more useful for the study of the steady-state solutions and their stability.

B. Spectral representation

Since, in the description of the bulk fluid hydrodynamics, Eqs. (2.1)–(2.3), we have neglected all nonlinear terms, these equations can be Fourier transformed analytically and reduced to a simpler form. Before doing that, however, we specialize to a specific geometry, namely, a two-dimensional capillary of size $L_x\times L_y$ with periodic boundary conditions in the x (flow) direction and impermeable walls at $y=0$ and L_y in the direction perpendicular to the flow. Since our system is finite in both directions, Fourier series are used and we have a discrete set of wave numbers. In the y direction we use a Fourier sine series for v_y, reflecting the boundary condition $v_y(\mathbf{r},t)=0$ at the walls. Once this choice has been made, the structure of Eqs. (2.1)–(2.3) determines the simplest choice for the other variables, namely, sine series for σ_{xy} and cosine series for v_x, σ_{xx}, σ_{yy}, and δp. The transformation of the equations is then performed by multiplying each equation by $\sin(k_y y)$ or $\cos(k_y y)$ and integrating with respect to y, where

$$k_y\equiv n\pi/L_y, \qquad (2.8)$$

with $n=0,1,2,\ldots$. For terms containing derivatives with respect to y, integration by parts is performed; care must be taken in considering the surface terms which turn out to be zero in all cases except in the equation for the propagation of v_x.

Straightforward manipulation of the resulting equations in Fourier space is then used to eliminate the variables $\delta p(\mathbf{k},t)$, $\overleftrightarrow{\sigma}(\mathbf{k},t)$, and $v_y(\mathbf{k},t)$, finally obtaining the following equation for $v_x(\mathbf{k},t)$:

$$\tau_m \frac{\partial^2 v_x(\mathbf{k},t)}{\partial t^2} + \frac{\partial v_x(\mathbf{k},t)}{\partial t} + \nu_0 k^2 v_x(\mathbf{k},t) = \frac{2\nu_0}{L_y}\frac{k_y^2}{k^2}[(-1)^n T_L(k_x,t) - T_0(k_x,t)] \tag{2.9}$$

for $k_y \neq 0$. For the special case $k_y=0$, $v_x(k_x,k_y=0,t)=0$ for $k_x \neq 0$ and

$$\rho \frac{\partial v_x(\mathbf{k}=0,t)}{\partial t} = -g(t) + \frac{1}{L_y}\sigma_{xy}(k_x=0,y,t)\big|_{y=0}^{L_y}. \tag{2.10}$$

In Eq. (2.9), $\nu_0 \equiv \eta_0/\rho$ is the kinematic viscosity [8] and we have defined a shear rate at the wall as

$$T_j(x,t) \equiv \partial v_x(\mathbf{x},t)/\partial y\big|_{y=j}, \tag{2.11}$$

where j takes on the value of y at the two walls: $j=\{0,L_y\}$. When we use a subscript on ψ or T to indicate at which wall the corresponding quantity is evaluated, we will replace L_y simply by L for notational simplicity. Note that the last term in Eqs. (2.9) and (2.10) arises from the aforementioned surface term that appears in the Fourier transformed version of Eq. (2.1).

$v_x(k_x=0,\ k_y=0,t)$ in Eq. (2.10) is simply the spatially averaged flow velocity in the die, which we will henceforth denote as $\overline{v_x}$. Experiments are typically run under conditions of either constant pressure or constant flow rate. The former condition is implemented by setting the pressure gradient $g(t)$ equal to a constant in Eq. (2.10). A constant flow rate is implemented simply by taking $\overline{v_x}$ equal to a constant, i.e., by requiring

$$\partial \overline{v_x}/\partial t = 0, \tag{2.12}$$

which from Eq. (2.10) implies that

$$g(t) = \frac{1}{L_y}\overline{\sigma_{xy}}(y,t)\big|_{y=0}^{L_y}, \tag{2.13}$$

where $\overline{\sigma_{xy}}(y,t)$ is the shear stress spatially-averaged along the flow direction. Henceforth, we will assume that Eq. (2.12) holds until we return to discuss constant pressure flow and a more complicated experimental flow condition in Sec. IV C.

We will consider ψ only in real space. Hence, Eqs. (2.4)–(2.7) remain essentially unchanged. Here, we simply rewrite them combining Eqs. (2.5)–(2.7) into one, specializing to our two-dimensional geometry, and incorporating the new notation we have introduced

$$v_x(x,y=j,t) = (-1)^{j/L_y} \ell \psi_j(x,t) T_j(x,t) \tag{2.14}$$

and

$$\tau \frac{\partial \psi_j(x,t)}{\partial t} = -c\psi_j^3(x,t) + b\psi_j^2(x,t) - a\psi_j(x,t) + (-1)^{j/L_y} H\sigma_{xy}(x,y=j,t) + \xi_0^2 \frac{\partial^2 \psi_j(x,t)}{\partial x^2}. \tag{2.15}$$

Finally, in order to obtain σ_{xy} appearing in Eq. (2.15), it is necessary to include Eq. (2.3) specialized to the shear component of the stress tensor at the walls

$$\tau_m \frac{\partial \sigma_{xy}(x,y=j,t)}{\partial t} = -[\sigma_{xy}(x,y=j,t) - \eta_0 T_j(x,t)]. \tag{2.16}$$

Equations (2.9) and (2.14)–(2.16) constitute a rewriting of Eqs. (2.1)–(2.7) in a mixed real space-Fourier space representation often more amenable for both analytic and numerical work. In what follows, we will make use of both the mixed and real space representations, according to which is more convenient for our purposes.

III. STEADY-STATE SOLUTIONS AND LINEAR STABILITY ANALYSIS

A. Steady-state solutions

The steady-state solutions are obtained from Eqs. (2.9) and (2.14)–(2.16) by setting all time derivatives equal to zero. We are interested in steady-state solutions that are uniform in the x direction, and thus have only the $k_x=0$ components of $v_x(\mathbf{k})$ and $T_j(k_x)$ nonzero. These components are simply the uniform-in-x real space values which we write succinctly as $v_x(k_y)$ and T_j. Explicitly summing the Fourier series for the y component to obtain the velocities in real space at the two walls, we can write Eq. (2.14) as

$$\ell \psi_0 T_0 = \overline{v_x} + \sum_{n=1}^{\infty} v_x(k_y) \tag{3.1}$$

and

$$-\ell \psi_L T_L = \overline{v_x} + \sum_{n=1}^{\infty} (-1)^n v_x(k_y), \tag{3.2}$$

where we recall Eq. (2.8) relating k_y and n. (It is worth noting that these equations also hold for a time-dependent state provided that it is uniform in the x direction.)

In the steady state, Eq. (2.9) reduces to

$$v_x(k_y) = \frac{2L_y[(-1)^n T_L - T_0]}{(n\pi)^2}. \tag{3.3}$$

If we substitute Eq. (3.3) into Eqs. (3.1) and (3.2), noting that $\Sigma_{n=1}^{\infty} 1/n^2 = \pi^2/6$ and $\Sigma_{n=1}^{\infty}(-1)^n/n^2 = -\pi^2/12$ [27], and solve for T_0 and T_L, we find that

$$T_0 = \frac{(\ell \psi_L + L_y/2)\overline{v_x}}{(\ell \psi_0 + L_y/3)(\ell \psi_L + L_y/3) - L_y^2/36} \tag{3.4}$$

and

$$T_L = \frac{-(\ell\psi_0 + L_y/2)\overline{v_x}}{(\ell\psi_0 + L_y/3)(\ell\psi_L + L_y/3) - L_y^2/36}. \tag{3.5}$$

Considering Eqs. (2.15) and (2.16) in the steady state and substituting in Eq. (3.4) and (3.5), the possible steady-state values of ψ_0 are given by the roots of a sixteenth-order polynomial. This polynomial factors into a fourth-order polynomial which gives those roots that describe steady states symmetric under reflection about the centerline of the capillary, and a twelfth-order polynomial describing the asymmetric steady states. Moreover, only six of the 12 asymmetric solutions are independent because the solutions must occur in pairs related by reflection about the midplane of the capillary.

The roots of the full sixteenth-order polynomial can be determined using standard numerical techniques [28]. For large enough slip length coefficient ℓ, the only physical roots (those with both ψ_0 and ψ_L real and positive) are the symmetric ones. To investigate these analytically, we note that when $\psi_0 = \psi_L$, Eqs. (3.4) and (3.5) reduce to

$$T_0 = -T_L = \frac{\overline{v_x}}{\ell\psi_0 + L_y/6}. \tag{3.6}$$

One can easily verify that this result agrees with the velocity profile obtained by a direct real-space calculation of the steady-state solution of the Navier-Stokes equation for pipe flow with the prescribed boundary conditions.

Considering Eqs. (2.15) and (2.16) in the steady state and substituting in Eq. (3.6), we obtain

$$c\psi_0^3 - b\psi_0^2 + a\psi_0 - \frac{H\eta_0\overline{v_x}}{\ell\psi_0 + L_y/6} = 0. \tag{3.7}$$

Upon multiplying Eq. (3.7) by the denominator of the last term, we have a fourth-order polynomial equation. The sign of the zeroth-order coefficient implies that the product of the four roots is negative, and therefore for given values of the parameters (and, in particular, fixed $\overline{v_x}$), we have the following three possibilities: (1) two complex-conjugate roots and two real ones, one positive and one negative; (2) three real positive roots and one real negative one; (3) three real negative roots and one positive one. Since only real positive roots are physical, we see the possibility of either one or three physical roots. The most relevant case of a flow curve which always has only one physical root is shown in Fig. 2(a).

For completeness, we show in Fig. 3 two unusual pathologies in the flow curve which can occur in our model for small values of the slip length coefficent but do not correspond, to the best of our knowledge, to any flow curves which have been observed experimentally. One pathology occurs when there is a region in $\overline{v_x}$ where Eq. (3.7) has three physical roots while the other occurs when asymmetric steady-state solutions appear in the region where the flow curve for symmetric solutions is nonmonotonic [29]. In all that follows, we will be interested in the case where the parameters of the model are such that the flow curve is like that shown in Fig. 2(a), i.e., with neither of these two pathologies.

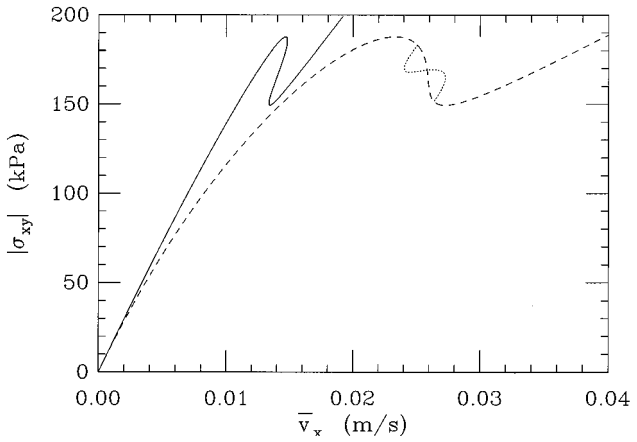

FIG. 3. Pathological flow curves which can be produced for different sets of parameters. The solid curve shows (the symmetric branch of) the flow curve when ℓ is reduced by a factor of 100 to $\ell = 0.0004$ m. Note that this curve is multivalued not only as a function of $\sigma_{xy}^{\text{wall}}$ but also as a function of $\overline{v_x}$. The dashed and dotted curve is for $\ell = 0.002$ m. The new branches of the curve (dotted) are ''asymmetric'' steady-state solutions, i.e., with different slip velocities at the two walls. [Such additional branches also occur for $\ell = 0.0004$ m, but have not been shown in order to illustrate the two types of pathologies separately.]

B. Linear stability analysis

Before studying the linear stability of the steady-state solutions, it is useful to consider qualitatively how the first-order transition in ψ, and the concomitant flow curve [cf. Fig. 2(a)], can lead to oscillations in the system. Consider the system with the polymer being pushed into the capillary at a flow rate where the slope of the flow curve is negative. The steady-state solution then has a value of ψ which is a maximum rather than a minimum of $f(\psi)$. Thus, we might naively expect that this solution is unstable. For the moment, we assume the fluid is sufficiently elastic that this instability still persists when the equation of motion for ψ is coupled to the equations of motion for the fluid. Then the kinetics of the first-order transition from small ψ (''stick'') to large ψ (''slip'') are the origin of oscillations in this regime: Consider the fluid initially in the stuck state. The stress along the walls will increase. At a critical stress, the stick state becomes metastable; at some stress beyond that [the spinodal, which is well-defined here because we have neglected noise in Eq. (2.6)], the stick state becomes absolutely unstable and the system jumps to the slip state. However, once in the new slip state, the stress at the walls decreases, the slip state itself eventually becomes metastable, and a transition to stick eventually ensues. Hence, the system can repeatedly cycle between stick and slip.

The range of $\overline{v_x}$ for which oscillations are expected to occur for any given parameter values can be determined analytically using linear stability analysis about the steady state. We consider linear perturbations to the steady-state values of the variables having the form

$$X(\mathbf{r},t) = e^{i(\omega t - k_x x)}\hat{X}(k_x, y, \omega), \tag{3.8}$$

where X has been used to denote a generic variable such as velocity, pressure, or ψ. First, substituting this form into Eq. (2.3) and defining

$$\nu_\omega \equiv \frac{\nu_0}{1+i\omega\tau_m}, \tag{3.9}$$

we find that

$$\delta\overleftrightarrow{\sigma} = \rho\nu_\omega \delta\overleftrightarrow{e}\,. \tag{3.10}$$

Here, and in the equations that follow, we omit the explicit functional dependences on k_x, y, and ω for brevity.

Next, substituting the form (3.8) into Eqs. (2.1) and (2.2), and using Eq. (3.10) and the fact that Eq. (2.2) allows us to write $\nabla\cdot\overleftrightarrow{e} = \nabla^2\mathbf{v}$, we obtain the following equations for the magnitude of the perturbed values $\delta v_x(k_x,y,\omega)$, $\delta v_y(k_x,y,\omega)$, and $\delta p(k_x,y,\omega)$:

$$\rho[i\omega+\nu_\omega(k_x^2-\partial_y^2)]\delta v_x = ik_x\delta p, \tag{3.11}$$

$$\rho[i\omega+\nu_\omega(k_x^2-\partial_y^2)]\delta v_y = -\partial_y\delta p, \tag{3.12}$$

and

$$-ik_x\delta v_x+\partial_y\delta v_y = 0. \tag{3.13}$$

Eliminating δp and δv_x from these three simultaneous linear equations then yields

$$[i\omega+\nu_\omega(k_x-\partial_y^2)][k_x^2-\partial_y^2]\delta v_y = 0, \tag{3.14}$$

which is valid for all $k_x \neq 0$. The solutions to Eq. (3.14) are linear combinations of $e^{q_j y}$ with $(q_1,q_2,q_3,q_4)=(k_x, -k_x,\kappa,-\kappa)$ and

$$\kappa \equiv \left(k_x^2+\frac{i\omega}{\nu_\omega}\right)^{1/2}. \tag{3.15}$$

However, because of the boundary conditions, Eq. (3.14) is an eigenvalue equation which can be satisfied only for particular linear combinations and accompanying discrete values of ω. Two conditions on the four coefficients are determined by the requirement that δv_y vanish at the two walls, which is easily satisfied by writing δv_y in terms of hyperbolic sine functions. The remaining two conditions are determined by using Eqs. (3.13) and (2.11) to obtain δv_x and δT from δv_y and then requiring Eq. (2.14) be satisfied at the two walls, i.e.,

$$\delta v_x(y=j) = (-1)^{j/L_y}\mathscr{\ell}(\overline{T_j}\delta\psi_j+\overline{\psi_j}\delta T_j), \tag{3.16}$$

where overbars are used to denote steady-state values. We can rewrite $\delta\psi_j$ in Eq. (3.16) in terms of δT_j by using the following expression derived from Eq. (2.15) with the help of Eq. (3.10):

$$[i\omega\tau+\overline{\chi_j}^{-1}+(k_x\xi_0)^2]\delta\psi_j = (-1)^{j/L_y}H\rho\nu_\omega\delta T_j\,. \tag{3.17}$$

Here, we have defined the inverse susceptibility by

$$\chi_j^{-1} \equiv \frac{\partial^2 f}{\partial\psi_j^2} = 3c\psi_j^2-2b\psi_j+a. \tag{3.18}$$

After some algebra, we find that the coefficients in the solution to Eq. (3.14) with the prescribed boundary conditions are nonzero only when ω satisfies the following condition:

$$\left[\overline{\psi_0}+\frac{H\rho\nu_\omega\overline{T_0}}{i\omega\tau+\overline{\chi_0}^{-1}+(k_x\xi_0)^2}-\frac{\nu_\omega}{i\omega\mathscr{\ell}L_y}h(k_xL_y,\kappa L_y)\right] \times\left[\overline{\psi_L}-\frac{H\rho\nu_\omega\overline{T_L}}{i\omega\tau+\overline{\chi_L}^{-1}+(k_x\xi_0)^2}-\frac{\nu_\omega}{i\omega\mathscr{\ell}L_y}h(k_xL_y,\kappa L_y)\right] = -\left[\frac{\nu_\omega}{\omega\mathscr{\ell}}\right]^2\left[\frac{k_x}{\sinh(k_xL_y)}-\frac{\kappa}{\sinh(\kappa L_y)}\right]^2, \tag{3.19}$$

where $h(x_1,x_2)\equiv x_1\coth(x_1)-x_2\coth(x_2)$.

Finally, specializing to the case of a symmetric steady state ($\psi_0=\psi_L$ and $T_0=-T_L$), Eq. (3.19) simplifies and we find, making use of Eq. (3.6), that the complex eigenfrequencies ω are given by the roots of

$$[\mathscr{\ell}\overline{\psi}+L_y/6][\mathscr{\ell}\overline{\psi}+L_yC_\pm(k_xL_y,i\omega L_y^2/\nu_\omega)] = \frac{-H\overline{v_x}\rho\nu_\omega\mathscr{\ell}}{i\omega\tau+\overline{\chi}^{-1}+(k_x\xi_0)^2}, \tag{3.20}$$

where we have defined

$$C_\pm(z,\zeta) \equiv \frac{\sqrt{z^2+\zeta}\left[\coth\left(\frac{1}{2}\sqrt{z^2+\zeta}\right)\right]^{\pm1}-z[\coth(z/2)]^{\pm1}}{\zeta}. \tag{3.21}$$

C_+ or C_- is used to obtain those eigenfrequencies corresponding to perturbations which are symmetric or antisymmetric with respect to reflection about the midplane of the capillary, respectively. Note that in Eq. (3.21), z is real but ζ is complex.

Since ζ is a function of ω, the exact stability equation contains transcendental functions of ω and thus can only be solved numerically. However, from Eq. (3.21), we find

$$C_\pm(z,\zeta\to0) = \frac{[\coth(z/2)]^{\pm1}}{2z}\left[1\mp\frac{z}{\sinh(z)}\right], \tag{3.22}$$

which is a good approximation for $C_\pm(z,\zeta)$ in the limit $|\zeta|\ll1$. Since $|\omega|$ is typically of order $1/\tau_m$, this can be understood as a condition that a typical hydrodynamic time scale for a viscous fluid, L_y^2/ν_0, be much smaller than the elastic time scale τ_m [25]. Using this approximation, Eq. (3.20) is quadratic in ω and we obtain the following four roots:

$$\omega=\frac{1}{2\tau_m}\left[i\left\{1+\frac{\tau_m}{\tau}[\overline{\chi}^{-1}+(k_x\xi_0)^2]\right\}\right.$$
$$\pm\left(\frac{4H\overline{v}_x\rho\nu_0\not{\psi}\tau_m/\tau}{[\not{\psi}+L_y/6][\not{\psi}+L_yC_{\pm}(k_xL_y,0)]}\right.$$
$$\left.\left.-\left\{1-\frac{\tau_m}{\tau}[\overline{\chi}^{-1}+(k_x\xi_0)^2]\right\}\right)^{1/2}\right]. \quad (3.23)$$

[In Eq. (3.23), unlike in Eq. (3.22) or previous equations, the signs indicated by the two $\pm$ symbols are allowed to vary independently.] In what follows, we assume the correctness of Eq. (3.23), and then return, at the end, to discuss how we expect the use of the exact expression to modify our results.

Referring back to Eq. (3.8), we see that instability occurs when any of the eigenfrequencies acquires a negative imaginary part. One can show from Eq. (3.23) that a necessary condition for instability is that the inverse susceptibility be negative, or in other words, that we be on the negative slope part of the flow curve in Fig. 2(a) [30]. Interestingly, however, this is not a sufficient condition. There are two cases, depending on the sign of the quantity in the square root of Eq. (3.23), or equivalently, whether or not the real part of ω is zero at the point where the imaginary part crosses zero. For the latter case, which seems to occur more generally (and, in particular, holds for the parameter values discussed in this paper, for all values of τ, τ_m, ξ_0, or k_x) [31] we can see from Eq. (3.23) that the condition for linear instability is simply given by the criterion

$$\overline{\chi}^{-1}+(k_x\xi_0)^2<\frac{-1}{(\tau_m/\tau)}. \quad (3.24)$$

Note that the dependence on $\overline{v_x}$ in Eq. (3.24) enters implicitly through $\overline{\chi}^{-1}$. In a recent paper, an instability was found by Georgiou [17] for a viscoelastic fluid in the Couette geometry. Georgiou assumed perfect stick at one wall and a highly nonlinear slip-stick boundary condition at the other such that the resulting flow curve was nonmonotonic, as in Fig. 2. This is related to our present treatment of Poiseuille flow, in the limits $\tau\equiv 0$ and $\xi_0\equiv 0$. However, within our model we find that the Couette flow case (with stick-slip transitions at both surfaces) will generically lead to additional branches of the flow curve involving asymmetric steady-state solutions analogous to those shown by the dashed and dotted curve in Fig. 3. This suggests a more complicated scenario where instabilities occur in some but not all regimes; in particular, we find evidence of linearly stable, but nonlinearly unstable, states. Further details of this work will be presented in a future communication.

Equation (3.24) shows that when $\overline{\chi}^{-1}$ become sufficiently negative, there will be an unstable band of wave numbers centered about $k_x=0$. The criterion for instability depends on the relative magnitudes of the elastic time scale, τ_m, and the time scale for relaxation of the conformation of the polymer at the surface, τ. The curves in Fig. 4 show the stability boundaries in the $\overline{v_x}$—$k_x\xi_0$ plane for various values of τ_m/τ as given by Eq. (3.24), while in the inset to Fig. 2 we have plotted the range of $\overline{v_x}$ for which the steady-state solution is unstable as a function of τ_m/τ (using the fact that $k_x=0$ is the most unstable wave number). We see that if

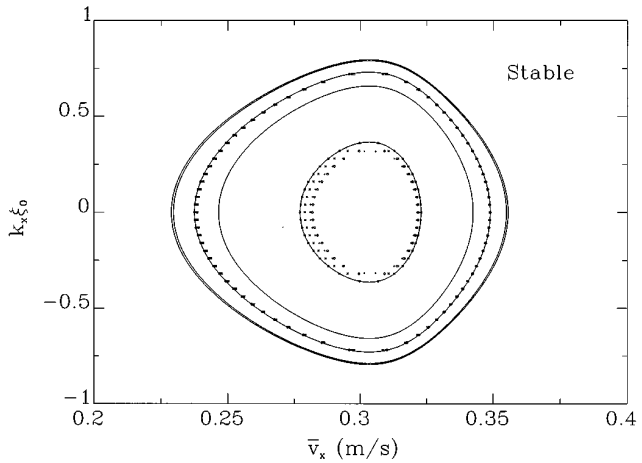

FIG. 4. Results of linear stability analysis. Solid curves show stability boundaries in the $\overline{v_x}$—$k_x\xi_0$ plane for $\tau_m/\tau=2$, 5, 10, 100, and 1000 (from inside curve to outside curve), computed using approximate criterion (3.24). For a given value of $\overline{v_x}$, the steady-state solution is predicted to be linearly unstable to all perturbations with dimensionless wave numbers $k_x\xi_0$ having values inside the boundaries shown. Points shown for $\tau_m/\tau=2$ and 10 give the exact stability boundaries obtained from the numerical solution of Eqs. (3.20) and (3.21) for a few different values of τ_m and ξ_0, including those values for which the deviations from the curves are most pronounced.

τ_m/τ is too small there is no instability for any $\overline{v_x}$. Instead, ψ at the walls relaxes to the steady-state value given by setting the left-hand side of Eq. (2.15) equal to zero. This is true even for $\overline{\chi}^{-1}<0$, when this steady-state solution of Eq. (2.15) alone [with σ_{xy} $(x,y=i,t)$ held constant at the steady-state value] is unstable, i.e., when the value of ψ at the walls corresponds to a maximum rather than a minimum of $f(\psi)$. Thus, as we would expect, the coupling to the viscous fluid produces a stabilizing effect on Eq. (2.15), but this stabilizing effect becomes weaker as the fluid becomes more elastic. This can be understood intuitively as follows: If the change in the polymer conformation occurs on a time scale τ which is short compared to τ_m then the fluid responds in an elastic (solidlike) manner and, in particular, has the ability to ''spring back.'' However, if the change in polymer conformation occurs on a time scale long compared to τ_m then the fluid responds in a viscous (fluidlike) manner and the oscillations are damped.

Note that, to the extent that criterion (3.24) holds, the stability is independent of any of the bulk hydrodynamic properties of the liquid besides τ_m [32]. Numerical investigations of our model to be presented in Sec. IV confirm the prediction of Eq. (3.24) that it is the ratio of the two relaxation times, τ_m/τ, which primarily determines the behavior; there is only very weak dependence of the behavior of the system on the value of τ_m for fixed τ_m/τ, provided that time is measured in units of τ_m.

We conclude this section with a few comments on the accuracy of our approximate stability criterion (3.24), given our use of Eq. (3.23) for the case where the real part of ω is nonzero at the stability boundary [31]. To test it against the exact analysis, we have used a nonlinear root-finding routine [28] to numerically solve for the roots of Eq. (3.20) using

Eq. (3.21) for various values of τ_m and ξ_0 at $\tau_m/\tau=2$ and 10, and a range of $k_x\xi_0$. The resulting stability boundaries are shown by the symbols in Fig. 4. We find that the symbols approach the curves in the limits $L_y^2/(\nu_0\tau_m)\to 0$, $L_y^2/(\nu_0\tau_m)\to\infty$, and $k_xL_y\to\infty$. That they seem to agree in these latter two limits in addition to the first one may at first seem surprising. It is because the arguments leading to Eq. (3.24) still hold to a good approximation even if we substitute $C_\pm(z,\zeta)$ for $C_\pm(z,0)$ in Eq. (3.23), provided that any imaginary part or any negative real part of $C_\pm$ is small [and that the real part of the entire term inside the square root in Eq. (3.23) remains positive]. In fact, one can show that the $z\to\pm\infty$ limiting behavior of $C_\pm(z,\zeta)$ is the same as $C_\pm(z,0)$ provided the additional requirement $z^2\gg|\zeta|$ is satisfied [33]. Conversely, for $|\zeta|\to\infty$ with $z^2\ll|\zeta|$, $C_\pm(z,\zeta)\to 1/\sqrt{\zeta}$ and thus $|C_\pm(z,\zeta)|$ becomes small, so $L_yC_\pm(z,\zeta)$ is only a small perturbation on the $\ell\psi$ term in Eq. (3.23).

Because the exact stability criterion agrees with Eq. (3.24) in all these limits, the actual stability boundaries never seem to deviate very far from those determined by Eq. (3.24). This can be seen in Fig. 4, where we have included the largest deviations that were found, which seem to occur roughly for $L_y^2/(\nu_0\tau)\approx 20$. We expect that other sets of parameters would show similarly small deviations.

Finally, we note that if we had assumed that the slip velocity is proportional to the shear stress rather than the shear rate of strain in Eq. (2.4) [21], then the effect would have been to multiply $\ell\psi$ in the *second* bracketed term of Eq. (3.20) by a factor of ν_ω/ν_0. This, in turn, makes the analysis somewhat more complicated, but the most general conclusions concerning the possibility of an instability when $\overline{\chi_0}^1<0$ remain unaltered. The approximate (3.24) is replaced by a more complicated criterion; however, in the limit $\tau_m/\tau\gg 1$, criterion (3.24) is again recovered.

IV. NUMERICAL RESULTS

Further investigation of our model is carried out numerically. We do this using the mixed real space spectral representation introduced in Sec. II. The infinite set of equations for $v_x(\mathbf{k},t)$ are reduced to a finite number by neglecting those beyond a maximum wave number in both k_x and k_y; for example, we restrict ourselves to $n\leqslant N_y$ in Eqs. (2.8) and (2.9). These equations, along with the real-space equations (2.14)–(2.16) discretized in the x coordinate, can then be propagated forward in time using Bulirsch-Stoer or Runge-Kutta routines for integrating ordinary differential equations [28]. We handle the second derivative in Eq. (2.15) by the standard discretization

$$d^2\psi/dx^2\to\frac{\psi(x_{i+1})+\psi(x_{i-1})-2\psi(x_i)}{(\Delta x)^2}. \tag{4.1}$$

Note that in Eqs. (2.14)–(2.16), the values of v_x and $\partial v_x/\partial y$ in real space are needed only at the walls and thus it is only there that numerical Fourier transforms need to be performed at each integration step. Since we use discrete Fourier transforms, the discretization in the x direction is related in a natural way to the cutoff in k_x: if the number of points used in real space is N_x, then the set of discrete wave numbers considered is $k_x=\{0,\pm 2\pi/L_x,\pm 4\pi/L_x,\ldots,\pm N_x\pi/L_x\}$, where the values of the function at the positive and negative wave numbers are complex conjugates of each other. Typical values used for the discretization were $N_y=15$–100; for N_x, we use $N_x=32$–2048, depending on the size of the structure present in the solution. For the ''one-dimensional'' case, where the system is forced to be uniform in the flow direction, we have checked that there is very good agreement between this mixed real-space-spectral method and a method employing real-space finite-differencing of the original partial differential equations.

TABLE I. Standard values chosen for various parameters. The last four parameters appear in the ψ^4 free energy, Eq. (2.7).

density	ρ	740. kg/m^3
viscosity	η_0	$1.\times 10^4$ Pa s
die width	L_y	0.004 m
slip length coefficient	ℓ	0.04 m
	a	5
	b	13
	c	10
	H	3.2×10^{-6} Pa^{-1}

The model has a large number of parameters and it is neither feasible nor useful to systematically investigate the effects of variations in all of them. Rather, the parameter values that we study are guided by experiment wherever possible. Except when otherwise noted, the values used are those given in Table I. For the material parameters ρ and η_0, we have chosen values typical of commodity polymers such as polyethylene. The parameters ℓ, a, b, c, and H, in Eqs. (2.14) and (2.15) are chosen so that steady-state solutions of the equations give a multivalued flow curve [Fig. 2(a)] typical of ones seen experimentally [1,2,23]. Since we have neglected shear thinning and our ψ^4 model is the most simplistic, we have only attempted to roughly reproduce experimental flow curves, rather than actually fitting our parameters to experimental data. We will find it instructive to investigate the model over various ranges of the phenomenological parameters τ, τ_m, and ξ_0, and the length of the capillary, L_x, but will also discuss what values we would expect these parameters to have in a typical experiment.

A. Spatially uniform solutions

We will first consider the limit $\xi_0\gtrsim L_x$, where the system is uniform in the flow direction. (For most experiments, this is probably not the relevant limit, since typical die lengths are on the order of 10^{-2}–10^{-1} m, while ξ_0 is expected to be a length on the order of polymer dimensions, i.e., on the order of 10^{-8} m, to at most 10^{-6} m. However the limit is still useful because it is simpler to study and serves as a start toward understanding the more complicated nonuniform regime.) In such a limit, we find that any initial nonuniformity of $\psi_j(x,t)$ along the walls decays away. Indeed, in order to study this limit most efficiently, we have often used a ''one-dimensional'' version of the code in which the flow direction is ignored altogether. This eliminates the need to perform Fourier transforms in the x direction; it also makes it unnecessary to specify the actual values of L_x and ξ_0.

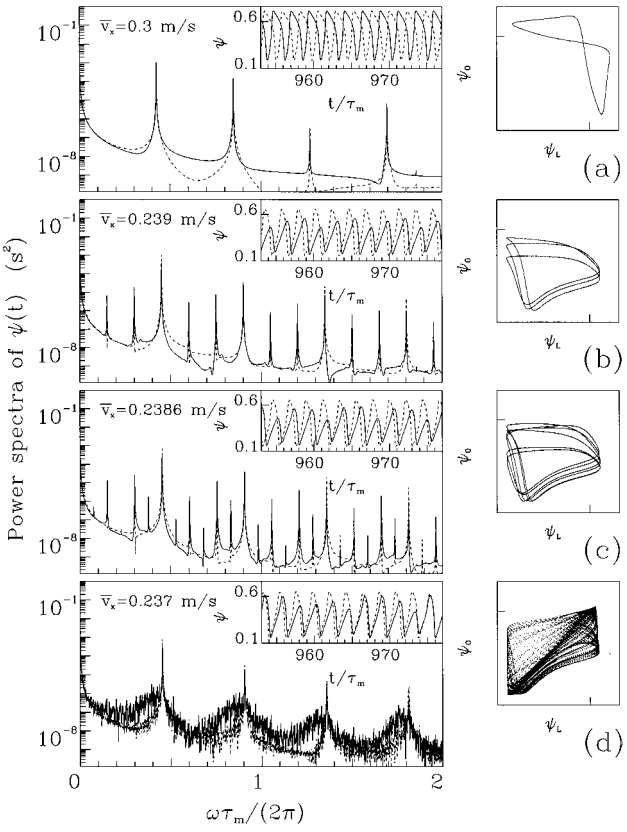

FIG. 5. Behavior of ψ_j at the two walls for $\xi_0 \gtrsim L_x$, at various flow rates all within the dashed region of the flow curve in Fig. 2. On the left, we present both time traces (insets) and power spectra (main graphs) of $\psi_j(t)$ for (a) period 1, (b) period 3, (c) period 6, and (d) chaotic oscillations. Walls at $y=0$ and L_y are indicated by solid and dashed lines, respectively. The graphs on the far right show phase space portraits, i.e., $\psi_0(t)$ vs $\psi_L(t)$ with time t treated as a parametric variable; the range for both axes is the same as that for the ordinate axis in the time traces. Parameters used are $\tau_m = 10^{-3}$ s, $\tau_m/\tau = 10$; the exact values of ξ_0 and L_x are not relevant.

The results of the linear stability analysis are confirmed by the numerics. In particular, the stability criteria for $k_x=0$ are in excellent agreement with where oscillating solutions first occur in our numerical simulations [34]. Some numerical results are shown in Fig. 5. The period of the oscillations is $O(\tau_m)$, increasing from within about a factor of 2 of τ_m in the limit $\tau_m/\tau \to \infty$ to several times τ_m when τ_m/τ becomes $O(1)$. There is also some dependence of the period on $\overline{v_x}$; except very near the stability boundaries, the tendency is for the period to become longer as $\overline{v_x}$ increases.

In order to make contact with experiment, it is necessary to estimate reasonable values for τ_m and τ. Eq. (3.24) expresses the approximate criterion for the ratio τ_m/τ in order that oscillations occur. It is generally believed that τ_m, which in a melt involves the dynamics of polymer entanglements, is proportional to the reptation time [35]. Since the stick-slip mechanism proposed by Brochard *et al.* [12,15] involves a large change in polymer conformation, the limiting factor is again likely to be polymer entanglements, and hence τ should also be proportional to the reptation time [25]. However, if a different physical mechanism is responsible for the stick-slip transition in some systems (for example, a surface adsorption-desorption mechanism, as has recently been suggested [14]), then the dependence of τ could be different. Clearly, the value of τ_m/τ relevant for experimental systems warrants further study. In most of our simulations, we have chosen $\tau_m/\tau=10$, which gives oscillations over most of the velocity regime where $\overline{\chi}^{-1}$ is negative with an oscillation period ranging from ~ 2.1 to $\sim 3.2\tau_m$ over the unstable regime of $\overline{v_x}$ using the parameters in Table I.

A definite value to use for the elastic time τ_m itself is likewise not easy to determine, since there is a large distribution of elastic time scales in polymeric materials [9]. However, considering the values obtained by Joseph, Riccius, and Arney for high molecular weight silicone oils using their shear wave speed meter [36], we believe that $\tau_m \approx 10^{-3}$ s should be a good order-of-magnitude estimate for long-chain polymer melts [37]. Such an estimate yields an oscillation period which corresponds reasonably well, given the flow rate, to the wavelength of experimentally observed sharkskin [3]. We thus believe that the viscoelastic oscillations that we observe correspond to the sharkskin texturing seen in experiments. This connection will be further elucidated below.

Over much of the unstable regime in $\overline{v_x}$, the oscillations are simple, with the two walls approximately 180° out of phase. However, for values of $\overline{v_x}$ which are close to the minimal and maximal ranges of the unstable regime [i.e., near the maximum and minimum in the flow curve of Fig. 2(a)], we find some of the more complex oscillatory behavior standardly seen in driven, damped nonlinear systems [38]. This includes chaotic behavior as well as oscillations with periodicities that are integer multiples of the fundamental oscillation period. For some values of $\overline{v_x}$, more than one stable attractor exists in the phase space and thus one finds different behavior depending upon the initial conditions. Sometimes the initial conditions can even determine whether or not the system oscillates at all [34]. Examples of the behavior seen are presented in Fig. 5. Note the period doubling in going from 5(b) to 5(c). Also, note that the phase space attractor need not be symmetric about the line $\psi_L(t)=\psi_0(t)$ [e.g., Fig. 5(b), 5(c), and 5(d)]; however, when it is not, the attractor related to this one by interchange of the two walls $[\psi_L(t) \leftrightarrow \psi_0(t)]$ is also a stable attractor.

As was noted above, the oscillations of ψ_j at the two walls are most often out of phase. Of course, in a real three-dimensional physical system, the walls of the container are not independent because they are connected to each other. Treating the two walls independently therefore describes the limit of a slit with an aspect ratio large compared to the length over which ψ is correlated perpendicular to the flow direction. In order to also simulate the other extreme, where the walls are forced to remain completely in phase, we have started the system with initial conditions in which $\psi(x)$ is equal at the two walls. Because there is no noise in the system to break this initial symmetry, this effectively enforces mirror symmetry in the system with respect to the centerline at $y=L_y/2$ for all times. Oscillations still occur in this case, although we have not found any of the more complicated behavior (larger period motion or chaos) that is present when $\psi(x)$ at the two walls varies independently.

Finally, we have performed some limited studies with a real-space finite-difference code that allows us to include

shear thinning in the model. We choose a local viscosity which varies with the magnitude of the local rate of strain tensor, $e \equiv (\frac{1}{2}\overleftrightarrow{e} : \overleftrightarrow{e})^{1/2}$, as

$$\eta(e) = \frac{\eta_0}{1+(e/e_0)^{1-n}}, \tag{4.2}$$

with, e.g., $e_0 = 1.4 s^{-1}$ and $n = 0.3$ [9]. The results suggest that the qualitative features described here remain unchanged, with the period of the oscillations decreasing as the shear thinning becomes more pronounced.

B. Spatially nonuniform solutions

Spatially uniform behavior in the flow direction (with either periodic or temporally chaotic motion) is the rule when L_x is small and ξ_0 is large; however, when ξ_0 is sufficiently small, the behavior can become quite complicated with more complicated structure, including what we believe to be spatiotemporal chaos [39], occurring. The behavior does not depend only on the ratio of L_x/ξ_0, since even for $\xi_0 = 0$, we find only uniform behavior for small enough aspect ratios L_x/L_y. This is because, as we will see below, the development of complicated structure involves the formation of velocity rolls and these rolls seem to have a minimum characteristic size on the order of the channel width L_y.

The behavior (at least over the times that we can measure it) also depends on the initial conditions. If we start the walls with only a small amount of nonuniformity [for example, variations in $\psi(x)$ of magnitude 10^{-3} or 10^{-2}] then for $L_x \lesssim L_y$ or $L_x \lesssim \xi_0$ we find that this nonuniformity decays. For larger L_x, the sort of behavior we get seems to depend on the behavior for the uniform case: If the value of $\overline{v_x}$ is such that the uniform case produces simple periodic behavior, then the variation along the walls remains small (but does not necessarily decay away completely as for smaller L_x). If the uniform case produces chaos or complicated periodic behavior, then we get spatiotemporal chaos.

The scenario is less clear when the initial condition has a larger amount of nonuniformity [for example, variations in $\psi(x)$ of magnitude 0.30]. In this case, the nonuniformity still decays for $L_x \lesssim L_y$ or $L_x \lesssim \xi_0$. However, for larger length capillaries, spatiotemporal chaos seems to be the rule, independent of the value of $\overline{v_x}$. This could be simply transient behavior, but it seems to be true out to times corresponding to several hundred oscillations with no indication that the nonuniformity along the walls is decaying.

The spatiotemporal behavior we see in $\psi_j(x,t)$ also manifests itself as complicated structures in the melt velocity inside the die. In particular, we see rolls spanning the die, Fig. 6(b), when we look at the velocity relative to the mean flow velocity, $\mathbf{v}(\mathbf{x},t) - \overline{v_x}\hat{\mathbf{x}}$. If there is only one roll across the width of the die, then the velocity at the two walls will be anticorrelated at any point along the die. Since the velocity is proportional to the slip length $\ell\psi_j(x,t)$ at the wall, this would be expected to lead to out-of-phase oscillations of $\psi_j(x,t)$ at the two walls [40]. In fact, there does generally seem to be one velocity roll across the capillary and the oscillations of $\psi_j(x,t)$ are most often out of phase [41]. That $\psi_j(x,t)$ at the walls in the two-dimensional capillary is most often out of phase correlates with the experimental fact that sharkskin in a cylindrical die often has a spiral pattern with opposite sides of the extrudate being out of phase.

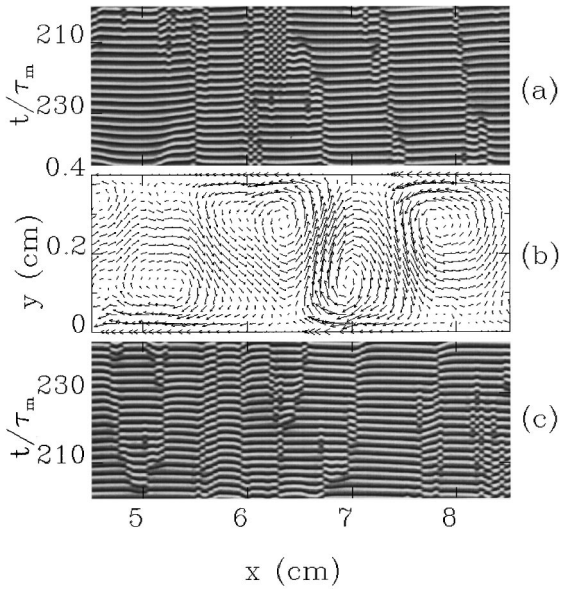

FIG. 6. Typical spatiotemporal patterns seen for $\xi_0 \ll L_x$. (a) and (c) show space-time plots of $\psi_j(x,t)$ along the top and bottom channel walls, respectively. The value of ψ_j is indicated by the brightness on this gray scale plot. (b) shows the flow pattern in the channel at the latest time in (a) and (c). Shown is the velocity relative to the mean flow velocity, $\mathbf{v}(x,y) - \overline{v_x}\hat{\mathbf{x}}$, with the magnitude (in arbitrary units) indicated by the size of the arrow. Note that the time increases from top to bottom in (a) in order to facilitate a comparison of the latest time in (a) with the top wall in (b). The defect structures evident in (a) and (c) are associated with the rolls in the channel shown in (b). Parameters used are the same as in the bottom panel of Fig. 5, except here $\xi_0 = 0$ m and $L_x = 0.1$ m. Note that only part of the channel has been shown in these figures.

Finally, we point out that the complicated spatiotemporal patterns at the two walls, shown in Figs. 6(a) and 6(c), have important experimental consequences: These, and analogous structures in the third dimension not included in our calculation, should manifest themselves as defects on the surface of the extrudate. Although no direct comparison can be made without including the third dimension in our model, we are encouraged by recent experiments [7] showing defect patterns on the surface of the extrudate (Fig. 7) similar to the patterns seen in the x-t plane in Fig. 6(a) and 6(c). (For other experimental pictures of the extrudate surface during sharkskin, see [3,42].)

C. Reservoir compressibility and nonuniform boundary conditions

In order to make closer contact with the experiment, two more features must be included in our model: (1) the compressibility of the polymer in the reservoir, and (2) the fact that the stresses are not constant along the die, but tend to be larger near the exit (and may also vary due to randomness produced, for example, by imperfections in the die itself), thus leading to nonuniform boundary conditions along the wall.

The inclusion of the extrinsic effect of compressibility in the reservoir is motivated by recent work [2,1] showing that

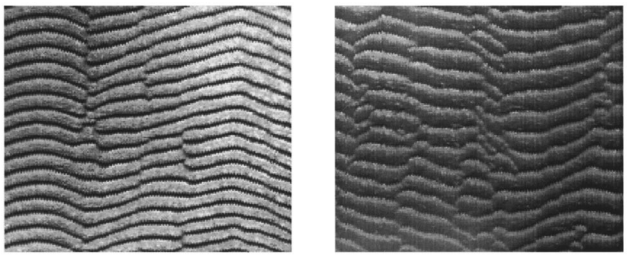

FIG. 7. The surface of linear low-density polyethylene extrudate at two different extrusion rates in the sharkskin regime from the experiment of Ref. [7]. Shown are gray scale plots of the height with white representing peaks and black representing valleys. The polymer melt was extruded in the upward direction, relative to the orientation of these images, out a slit die $\sim$0.15 m long with a rectangular cross section approximately 0.04 m $\times$ 0.002 m. The images show a region of the surface approximately 0.01 m across. Note that the patterns on the extrudate look qualitatively similar to the defect structures seen in Figs. 6(a) and 6(c).

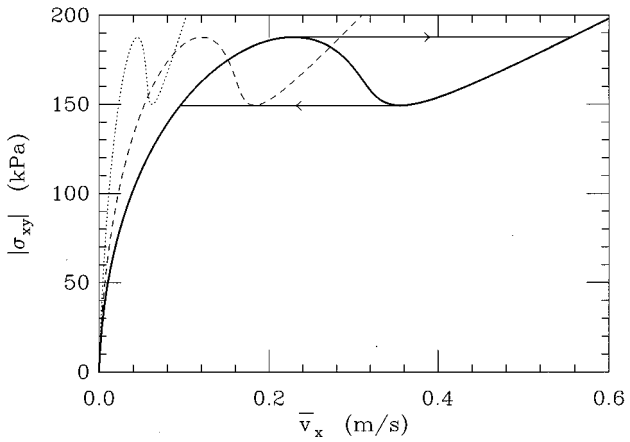

FIG. 8. The spurt flow regime. The bold solid curve shows our standard flow curve with $\ell = 0.04$ m. When reservoir compressibility is included and the piston speed is such that average flow rate is in the unstable part of the flow curve, the system cycles clockwise around the multivalued portion of the flow curve. The leftmost branch is the stuck part of the cycle and the rightmost branch is the slip part of the cycle; the horizontal solid lines show the rapid jumps between the stuck and slipping portions. The dashed, and the dotted curves are flow curves for $\ell = 0.04$, and 0.006 m, respectively. If we allow ℓ to vary along the wall of the capillary, then we will effectively have different flow curves in different regions of the capillary, with the possibility of interesting behavior as discussed in the text.

the long time-scale oscillations seen in the ''spurt'' regime are controlled by the volume and compressibility of the polymer in the reservoir, as had been suspected for some time [43]. This was demonstrated by showing that the flow rate exiting the die oscillates significantly in time and that experimentally the oscillation period for the spurt flow is proportional to the length of that part of the reservoir which contains the melt. In the case of Ref. [2], a model was also introduced in which the reservoir was considered roughly as a spring which coupled the constant velocity motion of the melt into the reservoir to the resulting varying rate at which the melt enters the die. It was found that the numerical results of this model well produced the experimental oscillations both in form and period.

The incorporation of reservoir compressiblity by considering the reservoir roughly as a spring [2] will give us one additional second-order differential equation for the average fluid velocity in the die; we will then see ''reservoir compressibility oscillations'' which have the expected linear behavior on the volume of polymer in the reservoir. Note that the inclusion of compressibility in the reservoir, while still ignoring it in the hydrodynamic equations we solve in the die itself, is reasonable: In most experiments, the volume contained in the reservoir is very large compared to the volume in the die and therefore a small change in the density of the polymer in the reservoir can lead to a change in volume in the reservoir which, though small on the scale of the reservoir, is large on the scale of the die.

The role of the reservoir can be explained qualitatively as follows: Let us consider the piston in the reservoir moving at a velocity v_R such that the steady-state flow velocity $\overline{v_x^0}$ in the die is in the unstable regime (in particular,

$$v_R A_R = \overline{v_x^0} A_d , \tag{4.3}$$

with A_R and A_d being the cross-sectional areas of the reservoir and die, respectively). If the die is first in the stuck state, then the flow rate and pressure in the die will be at some point near the leftmost branch of the multivalued flow curve shown by the bold solid curve in Fig. 8. Since material is being pushed by the piston into the reservoir faster than it is exiting the reservoir and entering the die, the density and pressure of the melt in the reservoir will increase. When this pressure exceeds the critical pressure given by the local maximum in the flow curve, the polymer at the wall in the die will change conformation and enter the slip state, and the flow rate in the die will jump to the right branch of the flow curve (as shown by the upper horizontal solid line in Fig. 8). However, at that point, the melt is now exiting the reservoir at a faster rate than the piston is forcing it, and thus the density and pressure of the melt in the reservoir (and die) decreases, until the local minimum in the flow curve is reached, at which point the polymer at the wall of the die reenters the stuck state, i.e., the system jumps back to the leftmost branch of the flow curve and the cycle repeats. Note that this scenario is similar in some respects to that which leads to the viscoelastic oscillations we discuss in the rest of the paper. The primary difference is that here it is the compressibility of the fluid in the reservoir rather than the fluid's shear elasticity that allows for the storage of energy. Also, because the volume of the polymer in the reservoir depends on details of the experimental design and on how much polymer remains in the reservoir, these oscillations are a less intrinsic part of the experiment than those leading to sharkskin. The final distinction is that this scenario leads to oscillations in the flow rate in the die, whereas when we considered only viscoelastic oscillations the flow rate was constrained to remain constant in the die (although the distribution of the velocity field across the die varied).

We now derive an approximate equation which governs this process. The approach is essentially the same as in Ref. [2] except that here we concentrate on the basic physics rather than including terms to get all the quantitative behav-

ior correct (e.g., shear-thinning effects, etc.). If we denote the mass of the polymer in the reservoir by M_R and the volume by V_R then the change in rate of change in mass in the reservoir can be written as

$$dM_R/dt = \rho dV_R/dt + V_R d\rho/dt. \tag{4.4}$$

Using the fact that $d\rho = \rho\beta dp_R$, where

$$\beta \equiv -(1/V)(dV/dp)$$

is the compressibility, and noting $dV_R/dt = -A_R v_R$ and $dM_R/dt = -\rho A_d \overline{v_x}$ (because the mass leaving the reservoir must be flowing into the die), we can rewrite Eq. (4.4) as

$$A_d(\overline{v_x} - \overline{v_x^0}) = -L_R A_R \beta \frac{dp_R}{dt}, \tag{4.5}$$

where we have made use of Eq. (4.3). Assuming that the pressure in the reservoir is given by the pressure at the die entrance [44], $p_R(t) = -g(t)L_x$, we can use conservation of momentum in the form [cf., Eq. (2.13)]

$$\rho \frac{d\overline{v_x}}{dt} = -g(t) + \frac{1}{L_y}\overline{\sigma_{xy}}(y,t)\Big|_{y=0}^{L_y} \tag{4.6}$$

to eliminate $p_R(t)$ from Eq. (4.5). After rearranging terms, this gives

$$\frac{d^2\overline{v_x}}{dt^2} + \frac{A_d}{A_R L_R L_x \rho\beta}(\overline{v_x} - \overline{v_x^0}) = \frac{1}{\rho L_y}\frac{d\overline{\sigma_{xy}}(y,t)}{dt}\Big|_{y=0}^{L_y}. \tag{4.7}$$

Equation (4.7) is an additional equation which must be integrated in time, replacing the trivial Eq. (2.12). It incorporates the effect of reservoir compressibility when an experiment is performed by regulating the speed of the piston.

We see that the effect of the compressibility is thus to make the flow rate in the capillary vary, even if the piston in the reservoir is pushed at a constant speed. Note that Eq. (4.7) is that for a driven harmonic oscillator. The driving term couples the oscillator to the equations we have already investigated. The oscillator is in a strongly driven regime where the relevant frequency of the spurt oscillations will be determined not simply from the natural frequency of oscillation in Eq. (4.7), but instead can be estimated very simply from the qualitative discussion of the origin of the oscillations given above: Consider the point as which the system has just jumped from the stuck to the sliding state. The time t that it takes for enough mass of material ΔM_R to drain through the die that the pressure is lowered sufficiently for the system to return to the stuck state is given by

$$t = \frac{\Delta M_R}{\rho A_d |\overline{\Delta v_x}|}, \tag{4.8}$$

where $\overline{\Delta v_x}$ is the average difference during the slipping part of the cycle between the (spatially averaged) velocity in the die and the average of the flow velocity in the die over an *entire* period, $\overline{v_x^0}$. A similar equation can be written down for the time it takes for mass to build up in the reservoir during the stuck part of the cycle, and the period $\mathcal{T}$ of oscillation is then equal to the sum of the two times. The quantity $\overline{\Delta v_x}$ is not easy to determine very precisely for either part of the cycle, but from Fig. 2(a) it seems that $\overline{\Delta v_x} \approx \overline{v_x^0}/2$ is a reasonable estimate to use for each part of the cycle [45]. Furthermore, $\Delta M_R = A_R L_R \Delta\rho$ where the change in density of the fluid is $\Delta\rho = \rho\beta\Delta p$. The pressure change Δp is determined from the difference in the wall stress $\Delta\sigma_{xy}$ between the local minimum and maximum in the flow curve: $\Delta p = 2\Delta\sigma_{xy} L_x/L_y$. Combining all this together gives us the following estimate for the period of the oscillations:

$$\mathcal{T} \approx \frac{8 A_R L_R L_x \beta \Delta\sigma_{xy}}{A_d \overline{v_x^0} L_y}. \tag{4.9}$$

Note that this formula has a very different dependence on various quantities (such as the volume of polymer in the reservoir) than would be derived by assuming that the period was the inverse of the natural oscillation frequency in Eq. (4.7); it agrees with the experimentally observed fact $\mathcal{T} \propto L_R$ [2] for spurt oscillations.

To study the effect of reservoir compressibility numerically, we must use values for the various parameters describing the reservoir dimensions and the melt compressibility. However, all these new parameters appear in Eq. (4.7) in one coefficient and thus there is only one new independent parameter that enters the equation. Noting that $\Delta\sigma_{xy} \approx 3.85\times10^4$ Pa for our flow curve in Fig. 2(a), using a reasonable materials value for the bulk compressibility of $\beta = 1.0\times10^{-9}$ Pa^{-1}, and choosing a reasonable value for the die length of $L_x = 0.1$ m, we can then consider the control parameter to be the ratio of the volumes of the reservoir and of the die, V_R/V_d. Figure 9 shows the observed oscillation period as a function of this control parameter for $\overline{v_x^0} = 0.30$ m/s, $\tau_m/\tau = 10$ and three different values of τ_m. We see that in the limit in which the volume of the reservoir is much larger than the volume of the die, the period of the oscillations in the die is controlled by reservoir compressibility and is in good agreement with Eq. (4.9). We find that these oscillations are in phase at the two walls, with large oscillations in the flow rate in the die. In the opposite limit in which the volume of the reservoir is much smaller than that of the die, the period of the oscillations in the die is controlled by the elasticity of the fluid, the oscillations are generally out of phase at the wall (and, can show chaotic behavior), with almost no oscillation in the flow rate in the die.

The two types of oscillations do not appear to coexist; In the limit where the reservoir compressibility oscillations dominate, the flow rate in the die switches rapidly from a small value to a large value, spending very little time at a flow rate in the unstable regime of the flow curve (see inset of Fig. 9). As a result, there is very little time to excite the elastic oscillations which thus show up only weakly, as a transient ''ringing'' effect in the velocity (and, to a much lesser extent, in ψ itself) following the transition between stick and slip. Thus, reservoir compressibility oscillations become the controlling phenomenon when they are included. By contrast, experiments show that sharkskin texturing can occur during part of the cycle in the spurt regime; furthermore, it also occurs at velocities below that at which the flow curve for the die appears to be multivalued at all.

To reconcile our model with the experimental observations, it is necessary to include one important feature of the

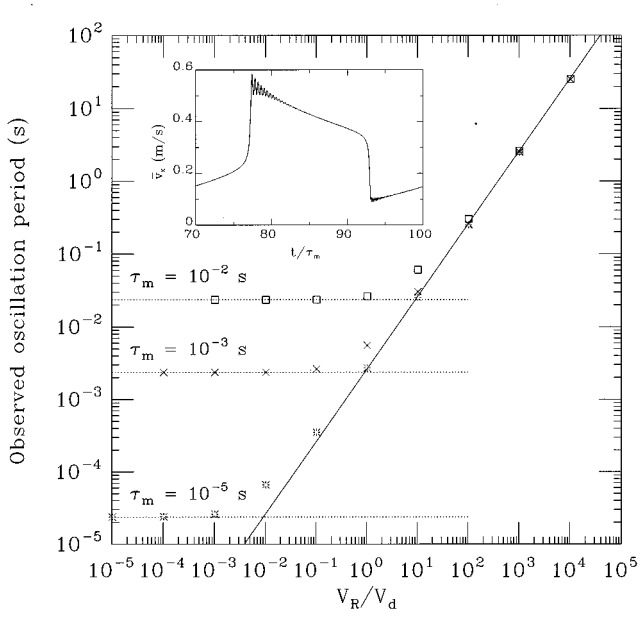

FIG. 9. Observed period $\mathcal{T}$ of the oscillations when the compressibility of the polymer in the reservoir is included, as a function of the ratio of the reservoir and die volumes, V_R/V_d. Parameters used are $\overline{v_x^0} = 0.30$ m/s, $\tau_m/\tau = 10$ and three different values of τ_m (top to bottom: $\tau_m = 10^{-2}$, 10^{-3}, and 10^{-5} s). In the limit where the reservoir is large, the oscillation period is in good agreement with the approximate formula for the period of reservoir compressibility oscillations, Eq. (4.9), shown by the solid line. In the opposite (less physical) limit, the oscillation period is determined by the elasticity of the fluid and is given by $\mathcal{T} \approx 2.37\tau_m$ (shown by dotted lines). The inset shows $\overline{v_x}(t)$ for about one complete oscillation for $V_R/V_d = 10$ and $\tau_m = 10^{-3}$ s. The flow rate in the die jumps very rapidly through the unstable regime and the only evidence of any oscillations at a period on the order of τ_m is the ''ringing'' effect following the jump. (We show here an unusually dramatic case; as V_R/V_d becomes larger, the time interval over which such ringing is observable becomes a much smaller part of the total cycle.)

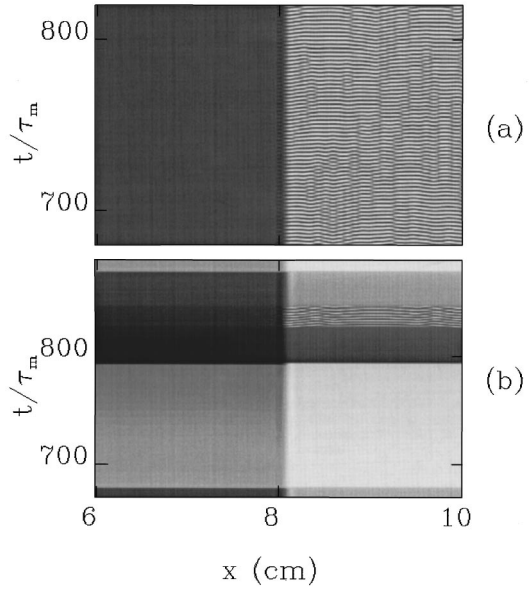

FIG. 10. Grayscale plots showing the magnitude of $\psi(x,t)$ at one of the two capillary walls, as a function of the position x along the wall and the time t, for the case where $\ell = 0.004$ m in 80% of the capillary and $\ell = 0.002$ m in the last 20%. Here, $\tau_m/\tau = 10$, $\tau_m = 10^{-5}$ s, and $V_R/V_d = 1$. The values of $\overline{v_x^0}$ are (a) 0.15 m/s and (b) 0.30 m/s. Note that only the last 40% of the capillary is shown.

system which has been neglected until now: the fact that die is not uniform and, in particular, that full solutions of the fluid flow equations with realistic constitutive laws show that higher stresses are present near the exit of the die [1,46]. We expect that the critical stresses at which the polymer conformation changes will be unaltered but that the flow rate at which such stresses are reached will be lower in the end region of the die. We can implement this most simply by assuming that a portion (''end'') of the die has a smaller slip length coefficient ℓ, cf. Eq. (2.14), and thus the flow curve for that region is shifted to the left of the primary flow curve (see Fig. 8).

For example, we assume that 20% of the die has an ℓ half that in the remainder of the die (see the dashed curve in Fig. 8). Of course, in the real system, ℓ might be expected to vary smoothly along the wall. However, the overlapping flow curves which we choose here should reproduce the most important aspects of the physics and will allow us to reproduce all the important features seen in experiments. In particular, they allow for the possibility of choosing flow rates at which the system is in a stable regime with respect to the primary flow curve but an unstable regime of the flow curve for the end of the die. It also allows for the possibility of more complicated behavior: at higher flow rates, the system is in the unstable regime for the primary flow curve and should execute reservoir compressibility oscillations which, during the stuck part of the cycle, will put the flow rate into the unstable regime of the flow curve for the end of the die. This allows the possibility of elastic oscillations superimposed on the reservoir compressibility oscillations during this part of the cycle.

Figure 10 shows us the expectations discussed above are indeed realized: For $\overline{v_x^0} = 0.15$ m/s, shown in 10(a), we see that the system does not execute compressibility oscillations since we are in the stable part of the primary flow curve, but that there are elastic oscillations in the end of the die where the system is in the unstable part of the flow curve. This is in agreement with the experimental fact that sharkskin is observed in a regime before spurt flow begins when the flow curve for the capillary as a whole is not yet multivalued. Furthermore, we find that this is true whether or not the polymer is pushed into the reservoir at a constant flow rate or a constant pressure (although, of course, which stable branch of the flow curve the system settles upon at a given pressure depends on the initial conditions). This is understood as follows: for an incompressible fluid, the average flow rate must be uniform along the length of the die. Hence, the stable flow in the majority of the die effectively enforces a constant flow rate through the end region even when the polymer is pushed into the die at a constant pressure. This behavior is again in agreement with experiment [2]: sharkskin is insensitive to whether the experiment is performed at constant pressure or flow rate.

For $\overline{v_x^0} = 0.30$ m/s, shown in Fig. 10(b), compressibility oscillations occur as expected. Furthermore, during the stuck part of the cycle, the flow rate spends a large amount of time

in the unstable regime of the flow curve for the end of the die and, as a result, elastic oscillations are set up in the end of the die. Indeed, experimentally, sharkskin is frequently observed on this part of the extrudate in the spurt flow regime [2].

In order to gain insight into how robust the behavior described above is, we have also considered several alternate choices for the variation in the value of ℓ along the die. For example, we have considered the case where the final 10% of the die has $\ell = 0.006$ m, producing the flow curve shown by the dotted line in Fig. 8. In this case, the behavior is qualitatively the same except that in the spurt regime we no longer see sharkskin superimposed. This is because, during the spurt oscillations, v_x never drops low enough to enter the unstable regime of the flow curve for the end of the die, as can be predicted by referring to Fig. 8.

A more realistic case would have ℓ varying continuously along the wall near the die exit from its value in the rest of the die to some smaller value; this continuous variation is expected to make the sharkskin behavior more robust since there will be a continuous distribution of local flow curves in the end region, with some overlapping the flow curve for the main part of the die such that simultaneous spurt and sharkskin are produced. As an example, we have investigated a system in which $\ell = 0.04$ m in 80% of the die and then decreases linearly to $\ell = 0.02$ m in 10% before increasing linearly back to $\ell = 0.04$ m in the final 10%. As we would expect, for $\overline{v_x^0} = 0.30$ m/s there are reservoir compressibility oscillations with viscoelastic oscillations at a given point in the last part of the die occurring when the flow rate is such that it is in the unstable regime for a flow curve with ℓ at the given value. Finally, in real systems, we expect that the walls will be quite inhomogeneous. To account for this, we have investigated a case where ℓ is chosen to have a random value between 0.02 and 0.04 m at each of the discretized points along the wall. For a given flow rate v_x^0 there are viscoelastic oscillations at those points along the die for which this flow rate falls in the unstable region of the local flow curve. Our general conclusions from all of these investigations are that the oscillatory behavior is quite robust and that the behavior at any point along the die can easily be understood in terms of simple arguments based on the nature of the local flow curve.

V. CONCLUSIONS

In summary, we have presented a model for the melt fracture instabilities seen in the extrusion of polymer melts. It includes a first-order transition between stick and slip behavior of the polymer at the walls as a function of the shear stress. The incorporation of the viscoelasticity of the fluid leads to oscillations. The system can in fact display very complicated spatiotemporal behavior which we suggest can explain sharkskin texturing. The additional incorporation of the extrinsic effect of the compressibility of the fluid in the reservoir allows us to obtain a unified description of both the sharkskin and spurt flow regimes seen in experiments.

The mechanism for the oscillations in our model is very simple—when the stress at the walls becomes too large, the polymers at the walls orient themselves so that slip occurs. This, in turn, results in a decrease in the stress at the walls which eventually causes the polymers to reorient themselves back to the stick condition. Provided that the fluid in the bulk responds to the change in boundary conditions in a sufficiently elastic manner, this scenario leads to oscillations of the fluid.

Finally, we should point out that we have not attempted here to model how the oscillations in the flow in the die translate into texturing on the surface of the extrudate. However, it seems clear that such oscillations should in general lead to features on the extrudate, particularly once the effects of variations in the normal stress [9] are considered. In future work, we hope to explicitly consider the behavior of the fluid once it exits the die. Such a study might be particularly useful in order to understand the gross melt fracture regime where the extrudate becomes most severely distorted.

ACKNOWLEDGMENTS

We thank Ken Elder and Rejean Ducharme for their collaboration in earlier stages of this work. We thank M. D. Graham for useful correspondence. This work was supported by the Natural Sciences and Engineering Research Council of Canada, and les Fonds pour la Formation de Chercheurs et l'Aide à la Recherche de Québec.

[1] M. M. Denn, Ann. Rev. Fluid Mech. **22**, 13 (1990).

[2] S. G. Hatzikiriakos and J. M. Dealy, J. Rheol. **36**, 845 (1992).

[3] D. S. Kalika and M. M. Denn, J. Rheol. **31**, 815 (1987).

[4] E. B. Bagley, I. M. Cabott, and D. C. West, J. Appl. Phys. **29**, 109 (1958).

[5] The apparent shear rate at the walls is derived directly from the flow rate under the assumption of the standard parabolic velocity profile of pipe flow. The actual shear rate at the walls can be very different due to shear thinning and wall slip.

[6] The phenomenology can be very complicated: not all the regimes are seen for all materials and there are dependences on such factors as molecular weight and polydispersity. The description we give here is that applicable to high-density polyethylene and some other long-chain linear (as opposed to branched) polymers.

[7] J. Tatibouët, R. Gendron, and L. Piché (unpublished).

[8] L. D. Landau and E. M. Lifshitz, *Fluid Mechanics*, 2nd ed. (Pergamon, Oxford, 1987).

[9] R. B. Bird, R. C. Armstrong, and O. Hassager, *Dynamics of Polymeric Liquids*, 2nd ed. (Wiley, New York, 1987), Vol. 1.

[10] J. J. Benbow, R. V. Charley, and P. Lamb, Nature **192**, 223 (1961); J. J. Benbow and P. Lamb, S.P.E. Trans. **3**, 7 (1963); F. N. Cogswell and P. Lamb, Trans. J. Plastics Inst. **35**, 809 (1967).

[11] P. G. de Gennes, C. R. Seances Acad. Sci. Ser. B **288**, 219 (1979).

[12] F. Brochard and P. G. de Gennes, Langmuir **8**, 3033 (1992); F. Brochard-Wyart, P. G. de Gennes, H. Hervert, and C. Redon, *ibid.* **10**, 1566 (1994); A. Ajdari, F. Brochard-Wyart, P. G. deGennes, L. Leibler, and M. Rubenstein, Physica A **204**, 17 (1994).

[13] P. P. Drda and S.-Q. Wang, Phys. Rev. Lett. **75**, 2698 (1995).

[14] Y. W. Inn and S.-Q. Wang, Phys. Rev. Lett. **76**, 467 (1996).

[15] K. B. Migler, H. Hervet, and L. Leger, Phys. Rev. Lett. **70**, 287 (1993); K. B. Migler, G. Massey, H. Hervet, and L. Leger, J. Phys. **6**, A301 (1994).

[16] G. C. Georgiou and M. J. Crochet, J. Rheol. **38**, 639 (1994); **38**, 1745 (1994).

[17] G. C. Georgiou, Rheol. Acta **35**, 39 (1996).

[18] J. D. Shore, D. Ronis, L. Piché, and M. Grant, Phys. Rev. Lett. **77**, 655 (1996).

[19] W. B. Black and M. D. Graham, Phys. Rev. Lett. **77**, 956 (1996), and references therein.

[20] J. D. Gunton, M. San Miguel, and P. Sahni, in *Phase Transitions and Critical Phenomena*, Vol. 8, edited by C. Domb and J. L. Lebowitz (Academic, London, 1983), p. 267.

[21] Alternatively, one could relate the slip velocity to the stress, rather than to the rate of strain, by replacing $\hat{\mathbf{n}}\cdot\nabla\mathbf{v}_\parallel$ by $\hat{\mathbf{v}}_\parallel\hat{\mathbf{v}}_\parallel\cdot\overleftrightarrow{\sigma}\cdot\hat{\mathbf{n}}/\eta_0$. (The division by η_0 allows us to preserve the interpretation of $\not{\psi}$ as a slipping length.) We discuss the implications of using this latter relation when we discuss the linear stability analysis in Sec. III B.

[22] P. C. Hohenberg and B. I. Halperin, Rev. Mod. Phys. **49**, 435 (1977).

[23] Specifically, we require that the parameters a, b, and c satisfy $3<b^2/(ac)<4$. For $b^2/(ac)<3$, no first-order transition occurs at all [i.e., $f(\psi)$ has only one minimum for all values of the shear], whereas for $b^2/(ac)>4$, $f(\psi)$ has two minima even when there is no shear. Positive values for b and H insure that the minima in $f(\psi)$ occur at $\psi>0$ for a shear stress such that the force of the fluid on the wall is in the same direction as the velocity.

[24] A full description of local polymer conformation would incorporate the polymer's random structure through a complicated order parameter. Furthermore, such a model could be applied throughout the fluid, with its local expectation value related to shear thinning. In fact, a scalar order parameter defined throughout the fluid has recently been used to study shear thinning in very small capillaries [M. Urbakh, L. Dalkhin, and J. Klafter, J. Chem. Phys. **103**, 10707 (1995) and references therein]. However, here we are interested only in that aspect of the conformation which is relevant in determining the slipping length.

[25] Because we will choose units of ψ such that the inverse susceptibility $\chi^{-1}\equiv\partial^2 f/\partial\psi^2$ is of order one, τ is a *macroscopic* time scale for an entire polymer to change its conformation rather than a microscopic dynamical time for polymer reorientation.

[26] In contrast to our model, in Ref. [16], only compressibility of the fluid is included, i.e., they consider a viscous Newtonian fluid with no shear elasticity. Also, because they have no intrinsic dynamics associated with their nonmonotonic slip condition at the walls, their simulation corresponds to taking the limit $\tau\to 0$ in our model and the negatively sloped region of their flow curve is always unstable. In a very recent paper, Ref. [17], their work has been extended to include shear elasticity. The constitutive law used therein decomposes the stress tensor into purely viscous and elastic parts; the purely viscous part of the shear viscosity plays a role somewhat analogous to our τ, allowing restabilization of part of the negatively sloped region of the flow curve.

[27] I. S. Gradshteyn and I. M. Ryzhik, *Table of Integrals, Series, and Products*, edited by A. Jeffrey (Academic, Orlando, 1980).

[28] W. H. Press, S. A. Teukolsky, W. T. Vetterling, and B. P. Flannery, *Numerical Recipes in C*, 2nd ed. (Cambridge University Press, Cambridge, England, 1992).

[29] For asymmetric steady states, the shear stress at the two walls is not equal and the vertical axis of Fig. 3 represents the average of the magnitude of these two stresses; alternatively, it simply denotes (up to a multiplicative factor) the pressure drop across the die.

[30] In general, $\overline{\chi}$ is negative on that section of the flow curve between the two horizontal tangents. This follows from the fact that $d\overline{\psi}/d\sigma_{xy}=H\overline{\chi}$ and that, since there is a term in the expression for $\overline{v_x}$ that is proportional to $\overline{\psi}$, $d\overline{v_x}/d\sigma_{xy}$ diverges at the same values of σ_{xy} as $d\overline{\psi}/d\sigma_{xy}$ does.

[31] When the crossing of the imaginary part of ω occurs with the real part zero, it will happen at a less negative value of $\overline{\chi}^{-1}$, i.e., the region of instability will be larger than predicted by Eq. (3.24). This seems to only occur for rather small values of τ_m/τ and is thus, in practice, often precluded by the system becoming completely stable. However, we have found a set of parameters (L_x increased to 0.04 m and $\tau_m/\tau=1.7$) where the crossing at higher $\overline{v_x}$ occurs with vanishing real part for some k_x, including $k_x=0$. Numerical solution of Eq. (3.20), for this case, shows that the boundaries of the instability region in the $\overline{v_x}$—$k_x\xi_0$ plane (which is small at any rate) do deviate a fair bit from those predicted by Eq. (3.24) and, for some values of ξ_0, the unstable region even becomes topologically more complicated, consisting of disconnected regions.

[32] In this limit where the hydrodynamics is unimportant, the linear stability analysis for our system is the same as that for the FitzHugh-Nagumo model, used to describe, e.g., neural excitation. [See A. Karma, Phys. Rev. Lett. **68**, 397 (1992); A. T. Winfree, Chaos **1**, 303 (1991); and references therein.] However, the full equations differ and, in particular, our more complicated system allows for the possibility of chaos even for a system which is spatially uniform (in the flow direction).

[33] It can easily be shown that $C_\pm(z)$ given by the approximate (3.22) is a strictly positive real function with the following limiting behaviors: $\lim_{z\to 0}C_+(z)=1/6$, $\lim_{z\to 0}C_-(z)=1/2$, and $\lim_{|z|\to\infty}C_\pm(z)=1/|2z|$.

[34] In fact, we sometimes see a subcritical bifurcation [38], whereby the oscillatory solution and a nonoscillatory solution are both locally stable in a narrow velocity regime. In this case, the stability analysis correctly predicts where the nonoscillatory solution becomes absolutely unstable.

[35] P. G. de Gennes, *Scaling Concepts in Polymer Physics* (Cornell University Press, Ithaca, N.Y., 1979).

[36] D. D. Joseph, O. Riccius, and M. Arney, J. Fluid Mech **171**, 289 (1986); **171**, 309 (1986); D. D. Joseph, *Fluid Dynamics of Viscoelastic Fluids*, Vol. 84 of *Applied Mathematical Sciences* (Springer-Verlag, New York, 1990); D. D. Joseph (private communication).

[37] In some of the numerical work discussed below, e.g., Fig. 10, we take advantage of the previously noted insensitivity of the behavior to the value of τ_m (for a fixed ratio τ_m/τ and with time measured in units of τ_m) and use $\tau_m=10^{-5}$ s since this

speeds up the numerical computations significantly.

[38] See, e.g., P. Bergé, Y. Pomeau, and C. Vidal, *Order Within Chaos* (Wiley, New York, 1984); H. D. I. Abarbanel, R. Brown, J. J. Sidorowich, and L. S. Tsimring, Rev. Mod. Phys. **65**, 1331 (1993).

[39] M. C. Cross and P. C. Hohenberg, Rev. Mod. Phys. **65**, 851 (1993); M. Caponeri and S. Ciliberto, Physica D **58**, 365 (1992); D. A. Egolf and H. S. Greenside, Nature **369**, 129 (1994).

[40] The proportionality between slip length $\not\psi_j(x,t)$ and velocity at the walls also involves the shear rate at the wall [see Eq. (2.14)], and thus the correlation between the two quantities need not be direct. In fact, we find that $\psi_j(x,t)$ can vary on shorter length scales than $v_x(x,y=j,t)$ does, although the variation in $v_x(x,y=j,t)$ does seem to roughly follow that of $\psi_j(x,t)$ with the latter coarse grained over a somewhat larger length scale, as can be seen in Fig. 6.

[41] The walls can behave symmetrically also, but this requires more than one roll across the channel, and so seems more difficult to create and sustain.

[42] M. T. Dennison, Trans. J. Plastics Inst. **35**, 803 (1967).

[43] A. P. Metzger, C. W. Hamilton, and E. H. Merz, S.P.E. Trans. **3**, 21 (1963); J. M. Lupton and J. W. Regester, Polym. Eng. Sci. **5**, 235 (1965).

[44] A better approximation would be to use Bernouilli's equation (Ref. [8]) to relate the pressures in the reservoir and in the die, thus incorporating the fact that pressure is lower in the die because of the higher velocity of the fluid. To lowest order, this introduces a nonlinear damping term of the form $(\overline{v_x}/L_x)(d\overline{v_x}/dt)$ on the left-hand side of Eq. (4.7). For the velocities of interest here, however, the effect of this term is expected to be very small; indeed we have found that numerical runs including this term differ negligibly from those which do not.

[45] For the stuck regime, one has the strict upper bound $|\overline{\Delta v_x}|<\overline{v_x^0}$. Note that the assumption that the times for the two parts of the cycle are equal is not a very good one when $\overline{v_x^0}$ is close to one of the edges of the unstable regime. In that case, Eq. (4.8) suggests, and numerical simulations confirm, that one or the other of the two times (and thus the total period $\mathcal{T}$) will become rather long.

[46] M. J. Crochet, A. R. Davies, and K. Walters, *Numerical Simulations of Non-Newtonian Flow* (Elsevier, Amsterdam, 1984); R. Keunings, in *Fundamentals of Computer Modeling for Polymer Processing*, edited by C. L. Tucker III (Carl Hanser Verlag, Munich, 1989), pp. 403–469; G. G. Lipscomb, R. Keunings, and M. M. Denn, J. Non-Newt. Fluid Mech. **24**, 85 (1987).